Kaleidoscopic Scintillation Event Imaging

Alex Bocchieri[1] John Mamish[2] David Appleyard[3] Andreas Velten[1]
[1]University of Wisconsin - Madison [2]Georgia Institute of Technology [3]Ubicept

https://bocchs.github.io/kaleidoscopic_scintillator

Abstract

Scintillators are transparent materials that interact with high-energy particles and emit visible light as a result. They are used in state of the art methods of measuring high-energy particles and radiation sources. Most existing methods use fast single-pixel detectors to detect and time scintillation events. Cameras provide spatial resolution but can only capture an average over many events, making it difficult to image the events associated with an individual particle. Emerging single-photon avalanche diode cameras combine speed and spatial resolution to enable capturing images of individual events. This allows us to use machine vision techniques to analyze events, enabling new types of detectors. The main challenge is the very low brightness of the events. Techniques have to work with a very limited number of photons.

We propose a kaleidoscopic scintillator to increase light collection in a single-photon camera while preserving the event's spatial information. The kaleidoscopic geometry creates mirror reflections of the event in known locations for a given event location that are captured by the camera. We introduce theory for imaging an event in a kaleidoscopic scintillator and an algorithm to estimate the event's 3D position. We find that the kaleidoscopic scintillator design provides sufficient light collection to perform high-resolution event measurements for advanced radiation imaging techniques using a commercial CMOS single-photon camera.

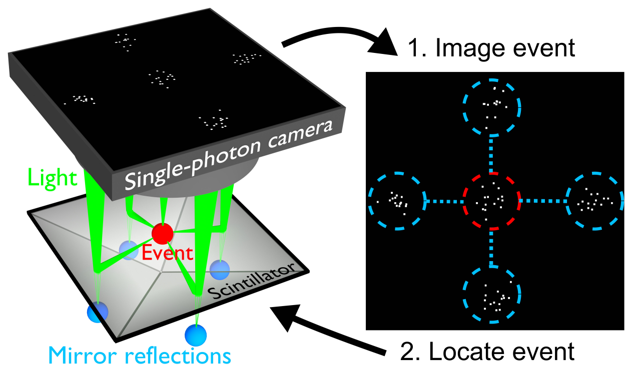

Figure 1. **Method overview.** An image is composed of light emitted from the scintillation event that reaches the camera either directly or after reflecting off mirrors of a kaleidoscopic scintillator. The spatial relationship between the event and mirror reflections is embedded in a Gaussian mixture model whose likelihood is maximized to estimate the event's location using the EM algorithm.

1. Introduction

High energy particles are created in nuclear processes including from man-made devices and natural interactions. There is a wide variety of particles with varying properties. Detecting and characterizing them is crucial for a broad range of applications including nuclear security [33], nuclear reactor and stockpile imaging [7], medical imaging [15], archeology [24, 30], and astronomy [31]. A particularly useful property of these particles is that many of them can penetrate through dense materials and therefore allow us to image through barriers and inside solid structures. The same penetrating properties, however, make it challenging to build a camera that can perform imaging or vision using high energy particles. A detector needs to have a large volume and density for a particle to interact. At the same time, we would like to know the location and shape of the interaction if it happens. One common approach to achieve this is by using a scintillator.

A scintillator is a transparent crystal that converts ionizing radiation into visible light. It provides mass for an incident particle to be absorbed and detected with a photosensor. While a particle is propagating through a scintillator, it may deposit energy and cause a "scintillation event". In the case of gamma-ray radiation, a gamma-ray collides with an electron in the scintillator and causes the electron to recoil over a random walk. A finite number of scintillation photons proportional to how much energy is deposited is emitted isotropically from the electron's path over a decay time. The photons propagate out of the scintillator and are captured by a sensor. Measurement of the event, such as its position, time, and energy deposition, is performed with the obtained signal. These measurements are then used in various downstream tasks to characterize the radiation source. Regardless of the task, optimizing light collection onto the sensor maximizes the signal to noise ratio (SNR) and event measurement performance (e.g. spatial, temporal, and energy resolutions).

This work focuses on optimizing imaging geometry in designs that estimate the 3D position of individual scintillation events with a single-photon camera. Currently, such designs estimate an event's 3D position using depth from defocus and perspective projection [8]. These designs suffer from low light collection and are susceptible to noise from dark counts. High-speed, single-photon sensors are required for tasks that measure individual events due to high particle incidence rates and the finite number of photons emitted by an event. For these kinds of tasks, increasing exposure time does not increase light collection per event and decreases SNR, which makes maximizing light throughput crucial. In general, large, thick scintillators are desirable because they increase the likelihood of events. However, estimating the 3D position of events in a larger volume is more challenging. Applications where 3D event locations are measured include the Compton camera [27], neutron scatter camera [34], positron emission tomography (PET), and single-photon emission computed tomography (SPECT) [15].

We propose a kaleidoscopic scintillator geometry with specular surfaces to increase light collection in a camera while preserving the event's spatial information. A kaleidoscope consists of planar mirrors oriented like a pyramid frustum that contains the object being imaged. Kaleidoscopes and light traps have been studied for imaging and reconstructing extended objects with abundant light [29, 35]. In this paper, we investigate the kaleidoscope as a technique for increasing light collection and reconstructing a point source in a photon-starved environment. We study the kaleidoscope in the context of scintillation event imaging and pose a radiation detection problem as a computer vision problem.

The image of an event in a kaleidoscopic scintillator contains direct light from the event and indirect light from the event's mirror reflections. Mirror reflections appear as events in locations determined by the event's location and the kaleidoscope's geometry, as illustrated in Fig. 1. The mirror reflections provide multiple views of the event and encode depth information with robustness to dark counts and low photon counts. Therefore, our proposed design improves event localization performance compared to previous non-kaleidoscopic methods. We introduce a Gaussian mixture model (GMM) in which the spatial relationships between the event and mirror reflections are embedded and an algorithm that estimates the event's 3D location via maximum likelihood. An overview of the method is shown in Fig. 1.

Our contributions are summarized as follows:

- A new scintillator design for increasing light collection in a camera while preserving the event's spatial information.
- Theory for modeling light from a kaleidoscopic event that arrives at the camera sensor.
- A probabilistic model of the image of a kaleidoscopic event with very few photons.
- An algorithm to estimate an event's 3D location in a kaleidoscopic scintillator. The algorithm is validated on experimental data captured with a single-photon avalanche diode (SPAD) camera and a gamma-ray source. Improved 3D localization performance is demonstrated on experimentally-calibrated simulations.

2. Related Work

Kaleidoscopic vision. Mirrors and kaleidoscopic designs have been used for stereo vision [13, 14, 26] and multi-view 3D reconstructions [2, 3, 6, 10, 20, 25, 29, 32] of an extended object using one picture from a single camera. A "light-trap" design consists of mirrors oriented such that light entering the trap reaches nearly every position inside the trap [35]. Time-of-flight is used to reconstruct a 3D object inside the trap. In fact, the pyramid-shaped light-trap was found to provide the best object coverage, which is the same shape as the kaleidoscope we use in this work.

Scintillation event measurement designs. Numerous designs exist for measuring scintillation events. Sensors such as silicon photomultiplier (SiPM) arrays or photomultiplier tubes (PMT's) can be coupled to the surface of a scintillator that is monolithic or pixelated with internal waveguides [15, 17, 19, 21, 22]. Camera designs measure events in a monolithic scintillator by imaging the scintillator with a lens [1, 4, 5, 8, 9, 12, 16, 23, 28, 36]. Using a camera to estimate the 2D position of an event in a thin scintillator, not including depth, is performed using center of mass algorithms [16, 18, 23].

There is limited work that estimates the 3D position of individual events with a camera. One work attempts to remove dark counts and estimate depth from defocus [8]. Another work uses stereo vision with two objectives and mirrors inside the imaging system to project two views of a cubic scintillator onto a hybrid photon detector [11]. Our proposed system provides multiple views, is more efficient, and uses a commercially available CMOS single-photon camera.

3. Kaleidoscopic Event Imaging Theory

We consider a square pyramid scintillator throughout this paper. Each face of the scintillator, except for the base, is a specular surface. The scintillator has an index of refraction

$n > 1$ and height h.

3.1. Imaging Configuration and Model

The world coordinate system's origin is set at the pyramid's apex with the z-axis directed perpendicular toward the pyramid's base surface. The camera coordinate system's origin is at the center of the lens with its z-axis directed toward the scintillator in the opposite direction of the world's z-axis. The x and y axes among the two coordinate systems are in the same direction. We denote a z-coordinate in the world coordinate system as z_w and camera coordinate system as z_c. Transforming between the two coordinate systems is done by subtracting the z-coordinate from the lens' z-coordinate in the world coordinate system. We use a thin lens to model the camera. Three planes to note are the focal plane, thin lens plane, and sensor plane. The focal plane is set at the apparent depth of the pyramid's apex at $z_w = h - h/n$. A thin lens with diameter A is placed at a distance S_1 from the focal plane. The sensor is placed at a distance S_2 from the lens. The lens' focal length is set to $f = (S_1^{-1} + S_2^{-1})^{-1}$. Parameters are illustrated in Fig. 2a.

Throughout this paper, the scintillator is oriented so that its base surface's edges are parallel with the sensor's respective edges. In this manner, the x-y dimensions of the normal vector for each specular surface of the scintillator are aligned along either the x or y axes. We denote the scintillator's four specular surfaces as +x, +y, -x, or -y mirrors.

A scintillation event is approximated as a point source of light emitting in all directions. Since the optical setup is constrained to short imaging distances, the images of an event and its mirror reflections exhibit defocus blur and have nonzero diameters. An image's diameter on the sensor varies according to the event's distance from the focal plane, following the circle of confusion model. Note that the camera sees an event at its apparent depth rather than its real depth due to the scintillator's index of refraction. An event's real and apparent locations are separated by $d - d/n$ along the z-dimension, where d is the event's real depth in the scintillator from the base surface. We denote an apparent location using the superscript "(a)" and a real location by the lack of a superscript. For an event at an apparent location $(x_0, y_0, z_{c0}^{(a)})$, the circle of confusion model yields

$$c = A \frac{S_2}{S_1} \frac{|S_1 - z_{c0}^{(a)}|}{z_{c0}^{(a)}} \quad (1)$$

where c is the image diameter at the sensor.

3.2. Mirror Reflections and Apertures

Consider the real location of an event at $\boldsymbol{p_0}$. Mirror k produces a mirror reflection with a real location at $\boldsymbol{p_k} = \boldsymbol{T_k}\boldsymbol{p_0}$ where

$$\boldsymbol{T_k} = \boldsymbol{I}_{3\times 3} - 2\boldsymbol{n_k}\boldsymbol{n_k}^T \quad (2)$$

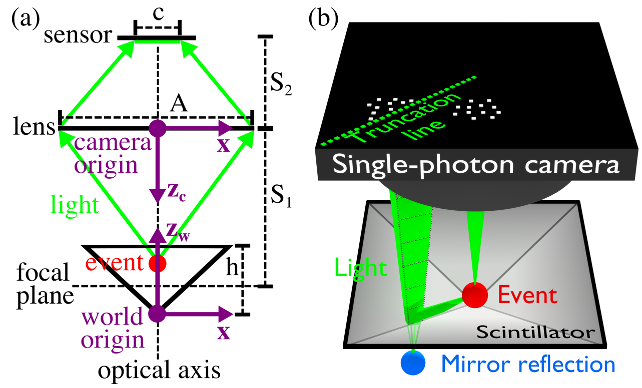

Figure 2. **(a) Imaging parameters and coordinate systems.** Only light emitted directly from the event to the camera is shown. **(b) Image truncation example in 3D.** The image of an event and one mirror reflection is shown. Light corresponding to the mirror reflection is truncated at the mirror's edge, resulting in a truncation line in the image. The truncation line only applies to that mirror reflection.

is the mirror's transformation, $\boldsymbol{I}$ is the identity matrix, and $\boldsymbol{n_k}$ is the mirror's normal vector. The mirror reflection of an event is also a point source of light. The captured image of the mirror reflection is obtained from the photons that reflect off the mirror and into the camera, exhibiting the same defocus blur as if an event were located at $\boldsymbol{p_k}$. However, due to the finite mirror size, the image on the sensor may be truncated along lines corresponding to the mirror's edges. This occurs when $\boldsymbol{p_k}$ is behind another mirror from the camera's perspective. The photons that are truncated from the image are those that reflect off the mirror adjacent to mirror k near the shared edge, as shown in Fig. 2b. Essentially, mirror k behaves like an aperture to a light source at $\boldsymbol{p_k}$. We denote the area on the sensor where photons from a mirror reflection cannot arrive as the "truncation zone" and its complement as the "acceptance zone". A line that separates the truncation zone and acceptance zone is a "truncation line". A 3D visualization of light truncation is shown in Fig. 2b. Supplementary Fig. 6 shows a 2D view of the propagation of light and how truncations form in various scenarios. Truncation lines are derived in Appendix A.

Light that reflects over multiple mirrors may be stopped by any of those mirrors' edges and also cause image truncations. We term a mirror reflection's "order" as the number of reflections its light underwent before forming. Light reflecting off mirror k can reflect off another mirror l and generate a mirror reflection at $\boldsymbol{p_l} = \boldsymbol{T_l}\boldsymbol{p_k}$. The light incident on mirror l from $\boldsymbol{p_k}$ passes through the aperture of mirror k. If this light spans a partial area A_l of mirror l, then mirror l's aperture is A_l. Otherwise, mirror l's aperture is simply the mirror. Mirror l's aperture affects the light emitted from $\boldsymbol{p_l}$ toward another mirror for a higher-order reflection and to-

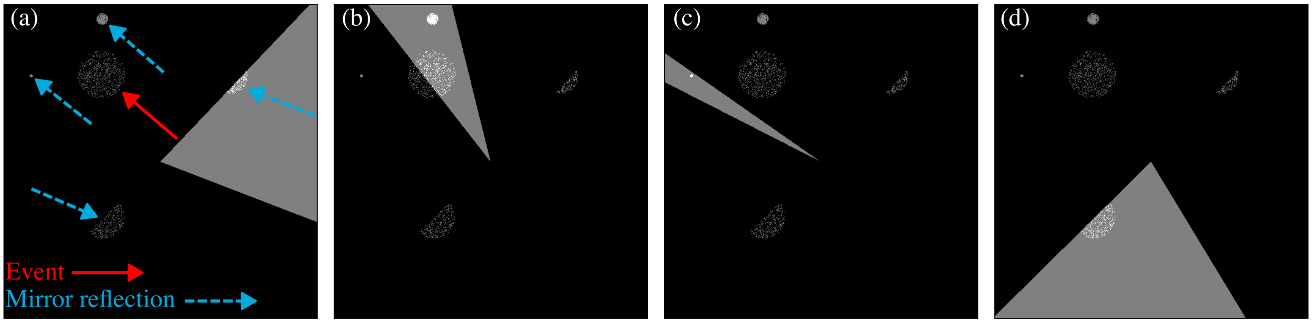

Figure 3. **Simulated kaleidoscopic image with theoretical acceptance zones.** Acceptance zones are derived for each mirror reflection and overlaid in gray on the image for the (a) +x, (b) +y, (c) -x, and (d) -y mirror reflections.

ward the camera for imaging. Higher-order reflections and imaging continue in the same manner.

3.3. Imaging Theory Validation

We validate the theory on mirror reflections and image truncations by observing that theoretically derived truncation lines align with photon arrivals in a simulated image. We simulate the image of an event in a kaleidoscopic scintillator in the shape of a square pyramid using a thin lens and ray tracing. We simulate an unrealistically high number of photons so that image truncations are clearly observable. Simulation details are in Appendix B. Acceptance zones for each mirror reflection are derived as in Appendix A and overlaid on the image. The resulting image is shown in Fig. 3.

4. Event Localization Algorithm

4.1. Image Model

We adopt a 2D Gaussian

$$\mathcal{N}(\boldsymbol{t};\boldsymbol{\mu},\sigma^2)=\frac{1}{2\pi\sigma^2}\exp\left(-\frac{||\boldsymbol{t}-\boldsymbol{\mu}||_2^2}{2\sigma^2}\right) \tag{3}$$

as the camera's point spread function and assume a circular Gaussian with covariance matrix $\boldsymbol{\Sigma}=\sigma^2\boldsymbol{I}_{2\times 2}$. $\sigma=ac$, where a is a proportionality constant determined by the optical configuration, and c is the circle of confusion diameter in Eq. (1). $\boldsymbol{t}$ is a 2D coordinate on the sensor plane.

An event or mirror reflection at apparent location $(x_k, y_k, z_{ck}^{(a)})$ is modeled as a point source of light, so its image on the sensor consists of photon arrivals spatially distributed over a 2D Gaussian with mean

$$\boldsymbol{\mu_k}=\left[\frac{S_2}{z_{ck}^{(a)}}x_k,\frac{S_2}{z_{ck}^{(a)}}y_k\right] \tag{4}$$

and standard deviation

$$\sigma_k=aA\frac{S_2}{S_1}\frac{|S_1-z_{ck}^{(a)}|}{z_{ck}^{(a)}} \tag{5}$$

where Eq. (4) is derived from perspective projection.

We model the image of an event in a kaleidoscopic scintillator with K mirror reflections and N photons as a GMM. The GMM has $K+1$ components that correspond to the event or a mirror reflection, and each photon in the image is a sample of the GMM. The location of each mirror reflection at $\boldsymbol{p_k}$ for $k=1...K$ generated from an event at $\boldsymbol{p_0}=(x_0,y_0,z_{w0})$ is known based on the kaleidoscope's geometry. For any mirror reflection k, each coordinate in (x_k,y_k,z_{wk}) is a linear combination of the event's (x_0,y_0,z_{w0}) coordinates based on the mirror's reflection transformation. All $\boldsymbol{p_k}$'s can be written in terms of $\boldsymbol{p_0}$ using Eq. (2), and each Gaussian component's $\boldsymbol{\mu_k}$ and σ_k can be written in terms of $\boldsymbol{p_0}$ by transforming to camera coordinates and using Eqs. (4) and (5). Thus, every Gaussian component is constrained to $\boldsymbol{p_0}$. This results in an optimization problem for estimating $\boldsymbol{p_0}$ that captures the global information of the event and all mirror reflections:

$$\underset{x_0,y_0,z_{w0},\boldsymbol{\pi}}{\text{argmax}}\ Q-\lambda\sum_{k=0}^{K}\left\|\boldsymbol{\mu_k}-\boldsymbol{\mu_k^0}\right\|_2^2 \tag{6}$$

where

$$Q=\sum_i\sum_k r_{ik}\Big[\log(\pi_k)+\log(w_i)-\log(2\pi{\sigma_k}^2)-\frac{w_i}{2{\sigma_k}^2}||\boldsymbol{t_i}-\boldsymbol{\mu_k}||_2^2\Big] \tag{7}$$

$$r_{ik}=\frac{\pi_k\mathcal{N}(\boldsymbol{t_i};\boldsymbol{\mu_k},\sigma_k^2)}{\sum_{k'=0}^{K}\pi_{k'}\mathcal{N}(\boldsymbol{t_i};\boldsymbol{\mu_{k'}},\sigma_{k'}^2)} \tag{8}$$

Q is the expected value of the weighted complete-data log-likelihood, r_{ik} is the probability of photon i belonging to component k given current parameter values, w_i is the weight assigned to photon i, π_k is the mixing weight for component k, $\boldsymbol{\mu_k^0}$ is the initialization point for $\boldsymbol{\mu_k}$

as described in the initialization procedure below, and λ is a regularization coefficient. We adopt a density-based weighting scheme for photon samples to minimize the influence of sparsely distributed dark counts and define $w_i = \sum_{j \in S_i^q} \exp\left(-\frac{||\boldsymbol{t_i} - \boldsymbol{t_j}||_2^2}{\nu}\right)$, where S_i^q is the set of q nearest neighbors of photon i, and ν is a positive scalar. We use the EM algorithm to optimize Eq. (6).

The above GMM formulation and definitions are derived in Appendix C. $\boldsymbol{p_k}$ is written in terms of $\boldsymbol{p_0}$ in Appendix I.1.

4.2. Optimization Algorithm

We assume a square pyramid kaleidoscope geometry, up to first-order reflections, and the presence of at least two mirror reflections in an image. Each edge of the scintillator's square surface is parallel to each respective edge of the sensor. In this configuration, mirror reflections' x-y coordinates will be located along either the $\pm x$ or $\pm y$ directions from the event's location.

One or more mirror reflections may be missing from the image due to truncations depending on the event's location. Therefore, determining which mirror reflections are present is required to compute Eq. (6). We run the following initialization procedure to determine the presence of mirror reflections and to initialize the event's estimated location for the EM algorithm.

Initialization procedure. The initialization procedure can be summarized as maximizing Eq. (6) over a set of possible event locations and $C \in \{3, 4, 5\}$ clusters (number of mirror reflections plus the event). First, centroids are computed using weighted KMeans with C clusters and the photons' assigned weights. Centroids are then classified as either the event, or $+x$, $-x$, $+y$, or $-y$ mirror reflections based on their relative positioning. This is done by taking combinations of subsets of centroids and computing the standard deviation of a subset's coordinates along the x and y dimensions to determine which centroids are horizontally or vertically aligned. We denote these centroids as $\boldsymbol{\mu_k^0}$. A set of possible event locations that is uniformly spaced over the depth (z dimension) of the scintillator is computed using the event's centroid and Eq. (4). The number of mirror reflections, which reflections are present, and the initialization point for $\boldsymbol{p_0}$ are those that correspond to the highest value of Eq. (6) out of this set and over $C \in \{3, 4, 5\}$. When computing Eq. (6), terms that correspond to a mirror reflection k are included only if that mirror reflection is determined to be present. $\boldsymbol{\pi}$ is initialized to the uniform distribution.

Optimization procedure. During the E-step, r_{ik} is updated using Eq. (8) and the current values of $\boldsymbol{p_0}$ and $\boldsymbol{\pi}$. If photon i is distant from any $\boldsymbol{\mu_k}$ and computing the denominator in Eq. (8) results in underflow, then we set $r_{i:} = 0$ and do not use photon i in computations. During the M-step, $\boldsymbol{p_0}$ is updated by fixing $\boldsymbol{\pi}$ and optimizing Eq. (6) with gradient ascent. The gradient with respect to $\boldsymbol{p_0}$ is derived in Appendix I. $\boldsymbol{\pi}$ is then updated using $\pi_k = \frac{1}{N}\sum_{i=1}^{N} r_{ik}$. In both the E and M steps, terms that correspond to a mirror reflection k are included in the computation only if that mirror reflection is present in the image.

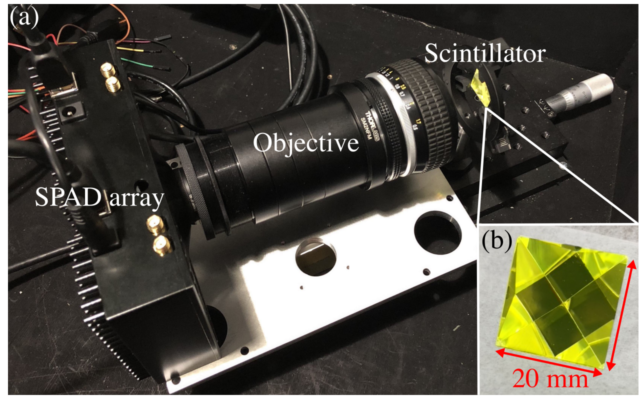

Figure 4. **Experimental setup.** (a) The setup without the gamma-ray source. (b) The kaleidoscopic scintillator.

Regularization. We introduce the regularization term $\lambda \sum_{k=0}^{K} \left\|\boldsymbol{\mu_k} - \boldsymbol{\mu_k^0}\right\|_2^2$ to favor solutions where all components' $\boldsymbol{\mu}$'s are close to their corresponding $\boldsymbol{\mu}^0$. This regularization is most helpful in cases where the mirror reflection photon clusters are close to each other. Without regularization, the algorithm may find an optimum that groups the event and one or more mirror reflections together into one component with a large σ while having other components' $\boldsymbol{\mu}$'s that do not coincide with a photon cluster. An example of this is shown in Supplementary Fig. 11.

5. Hardware Experiments

Hardware and data collection. The experimental hardware consists of a SPAD array, lens, scintillator, and 1 μCi Co-60 gamma-ray source (1.17, 1.33 MeV). We use the SPAD512 (Pi Imaging) array with microlenses for increased fill factor, which has 512×512 pixels and 16 μm pixel pitch. The lens is a 50 mm focal length Nikkor lens set to a f/1.2 aperture. We use a GAGG(Ce)-HL scintillator (Epic Crystal), which has a 150 ns decay constant, a 530 nm emission peak, and an index of refraction of 1.91. Its geometry is a square pyramid with a 20 mm wide base, 5.77 mm height, and a 120 degree opening angle at the apex. This wide angle is chosen so that second-order reflections are unlikely to occur or be imaged. Four surfaces of the scintillator are coated with enhanced specular reflector. The SPAD array is configured to capture 1-bit images with 1.5 μs integration time to minimize the accumulation of dark counts while allowing time for scintillation light to be emitted. The camera's lateral field of view (FOV) covers approximately 5.5×5.5 mm at the focal plane. The scintillator is positioned such that its apex is in-focus and centered in the camera's FOV,

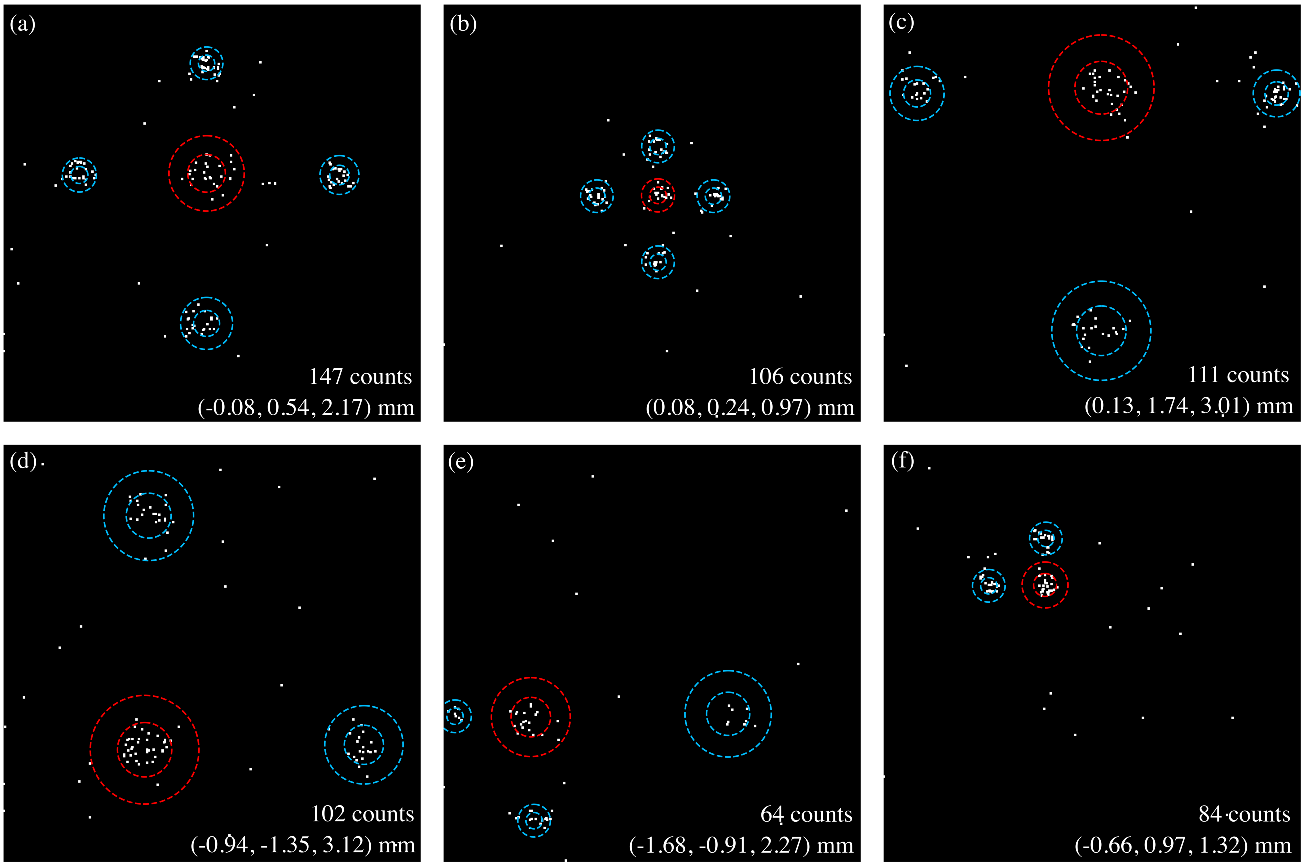

Figure 5. **Selected experimental images.** Experimental images overlaid with the algorithm's estimated Gaussian components. Each dashed circle is centered on the Gaussian component's mean. The inner and outer circles are one and two standard deviations in radius, respectively. Red and blue circles represent the event and mirror reflections, respectively. Pixels with a photon are enlarged with a 3×3 filter for visualization purposes. The number of counts in the image and the algorithm's estimated event location are shown in each image.

and that the scintillator's base edges are parallel with the sensor's respective edges. An air gap of approximately 30 mm exists between the scintillator and the lens. The entire setup is placed inside a light-tight enclosure to keep ambient light out. The experimental setup and scintillator are shown in Fig. 4. The experimental camera focus is shown in Supplementary Fig. 16.

Data collection took place at about 21 degrees Celsius ambient temperature. We first captured 130,000 images without the gamma-ray source to compute a mask of 5% of pixels with the highest dark count rates. We zero the pixels in this mask in all experimental images. After zeroing 5% of pixels, we observe a median of 4 dark counts per image. A histogram of dark counts per image is shown in Supplementary Fig. 9.

We collect data with the the gamma-ray source placed adjacent to the scintillator's apex and passively capture images since the timing of gamma-ray emissions cannot be controlled. All computations are performed in post-processing. We capture 13,000,000 images with the gamma-ray source present and discard images with less than 60 counts, resulting in 4,379 images. Histograms of counts in an image are shown in Supplementary Fig. 10.

Parameter values. In all experiments, we set $\lambda = 10$. We clip all σ_k's to a a minimum value of 10 pixels to account for imperfect focusing and a non-ideal point source, and to prevent singularities. The gradient of σ_k is set to 0 if σ_k gets clipped to the minimum value. See Appendix D for the values of all the algorithm's parameters and Appendix E for how camera parameters are calibrated.

Kaleidoscopic image model validation. We select six experimental images and overlay the algorithm's estimated Gaussian components, shown in Fig. 5, to validate the presence of mirror reflections in accordance with the kaleidoscopic model. Additional experimental images are shown in Supplementary Fig. 13.

Localization algorithm cross-validation. Experimental events cannot be controlled, so their ground truth locations are unknown. Therefore, to validate that the algorithm is measuring the event's location, we report agreement of multiple measurements of the event's location as follows. We use experimental images that contain the event and four mirror reflections as test images. The number of mirror reflections in an image is determined using the algorithm's initialization procedure. Then, we create new images of the event by removing combinations of one or two mirror reflections from the image. Photon i is classified as belonging to mirror reflection k according to $\max_k r_{ik}$ using r_{ik} values obtained after running the algorithm's optimization procedure on the original test image with four mirror reflections. Thus, for one test image, we generate 4 images with one mirror reflection removed and 6 images with two mirror reflections removed for a total of 11 images corresponding to one event. We run the algorithm's initialization and optimization procedures on each image to obtain 11 measurements of the event's location. We compute the mean estimated event location over the 11 images corresponding to one event. We record the distance between the mean location and the estimated location for each individual image. The distribution of this distance over all images is used to report the agreement in event location measurements, where short distances indicate good agreement. This metric also provides a measure of experimental precision. Selecting images by using the algorithm that contain four mirror reflections and at least 60 counts resulted in 1,606 test images. The median, mean, and standard deviation, respectively, of distances are 0.10 mm, 0.17 mm, and 0.22 mm over 17,666 distances. Distances are reported in a histogram in Supplementary Fig. 14.

To confirm that mirror reflections are being correctly identified and removed, we record the fraction of photon counts in an image that are removed. We assume that an event and each mirror reflection have the same average brightness. Therefore, we expect about 1/5 and 2/5 of counts in an image to be removed when removing one and two mirror reflections, respectively. The median, mean, and standard deviation, respectively, of the fraction of counts removed in an image are 0.19, 0.18, and 0.07 over 6,424 images where one mirror reflection has been removed, and 0.38, 0.37, and 0.08 over 9,636 images where two mirror reflections have been removed. The distribution of fractions of counts removed are reported in histograms in Supplementary Fig. 15.

Regularization ablation study. We perform an ablation study to demonstrate the effectiveness of regularization in Eq. (6). Details are in Appendix F.

6. Simulations

Comparison to prior art. Since scintillation events are difficult to produce at controlled locations, direct evaluation of the method requires simulated data. Here, we simulate our system and compare its localization performance to prior 3D localization methods, which estimate depth from defocus in the absence of mirror reflections [8]. We evaluate position accuracy and resolution over a grid of event locations and over different levels of event brightness. We use the same scintillator geometry, index of refraction, calibrated camera parameter values, and sensor array specifications as in the experiments.

		Average error and resolution (mm) ↓			
N_0	Algorithm	3D Error	x Res.	y Res.	z Res.
30	Kaleid. (ours)	**0.14**	**0.16**	**0.14**	**0.14**
	Non-kaleid. (ours)	0.83	1.36	1.41	1.32
	Noise-removing [8]	0.64	1.04	1.02	1.04
20	Kaleid. (ours)	**0.16**	**0.15**	**0.17**	**0.16**
	Non-kaleid. (ours)	0.79	1.17	1.24	1.21
	Noise-removing [8]	0.68	1.05	1.03	1.06
10	Kaleid. (ours)	**0.29**	**0.27**	**0.31**	**0.27**
	Non-kaleid. (ours)	0.95	1.36	1.33	1.28
	Noise-removing [8]	0.80	1.20	1.13	1.14

Table 1. **Simulation results.**

Image generation. For a given event location, we generate 100 kaleidoscopic images for each of three brightness levels as follows. We compute the locations of the mirror reflection and draw $Poisson(N_0)$ photons from each Gaussian component parameterized according to Eqs. (4) and (5) and accounting for the index of refraction. As in the experiments, all σ_k's are clipped to a minimum value of 10 pixels, which corresponds to $z_w = 0.82$ mm with the given experimental parameter values. Acceptance zones are computed, as described in Appendix A, and photons that lie outside their mirror reflection's acceptance zone are removed. We test brightness levels over $N_0 \in \{10, 20, 30\}$. $Poisson(10)$ dark counts are uniformly randomly added over each image. At each location, we also generate 100 non-kaleidoscopic images in the same manner, except that no mirror reflections are generated.

Event locations. The grid of event locations spans $x \in (0, 2.5)$ mm, $y \in (0, 2.5)$ mm, and $z_w \in (0.82, 3.5)$ mm. This grid is selected so that event locations span one x-y quadrant due to the system's symmetry, and σ_0 corresponding to the event's photon cluster is above the minimum clipping threshold. Grid points are equispaced over 10 points in each dimension. If less than two mirror reflections' centroids ($\boldsymbol{\mu_k}$'s) are in their acceptance zones and within the sensor, then the event location is discarded. These discarded locations correspond to points near the edge of the camera's FOV, and we consider their resulting image to be inadequate for applying our proposed algorithm. Event locations that lie outside the scintillator are also discarded. This results in a total of 463 valid event locations.

Algorithms. The proposed algorithm is tested on the kaleidoscopic images with the same parameter values and initialization and optimization procedures as on the experimental data. A non-kaleidoscopic version of the proposed algorithm is tested on non-kaleidoscopic images. The non-kaleidoscopic version of the algorithm is the same as the kaleidoscopic version, except that initialization points are lower-bounded at $z_w = 0.82$ mm, only one cluster or Gaussian component is computed, and $r_{ik} = \mathbb{1}\{k = 0\}$ for all photons.

We also test a prior method on non-kaleidoscopic images that attempts to classify and remove dark counts and then directly solve for the event location's maximum likelihood estimate without weighting photons [8]. More details of this method are in Appendix G. The algorithms that are applied to non-kaleidoscopic images estimate depth from defocus.

Performance metrics. At each location, we compute the mean 3D error (Euclidean distance) over all images and the spatial resolution. Spatial resolution is defined as $2.355\sigma_e$ (full width half maximum), where σ_e is the standard deviation of one dimension of the estimates of an event location. We report the averages of the mean 3D error and the spatial resolution in each dimension taken over all event locations for each brightness level $N_0 \in \{10, 20, 30\}$ for the three different algorithms. Tab. 1 contains results for the kaleidoscopic and non-kaleidoscopic versions of the proposed algorithm and for the prior method with $T_{edge} = 80$ pixels (see Appendix G for details). The prior method's results using different T_{edge} values are reported in Supplementary Tab. 2.

7. Discussion

Simulated validation of theoretical image truncations. The mirror reflection images generated with ray tracing and a thin lens are truncated along the theoretically derived acceptance zones, shown in Fig. 3. This suggests the theoretical models for mirror reflection locations and image truncations are correct. In Fig. 3, the +x and -y mirror reflections are partially truncated, while the +y and -x mirror reflections are not truncated.

Experimental validation of kaleidoscopic image model. Various examples where the Gaussian components predicted by the algorithm coincide with the photon clusters of the event and mirror reflections are shown in Fig. 5. This demonstrates that mirror reflections are indeed being captured in accordance with the proposed model. Examples include events occurring at high (Fig. 5a) and low (Fig. 5b) z_w-coordinates, mirror reflections lying outside the FOV (Fig. 5c,d), and mirror reflections that are completely truncated (Fig. 5e,f).

Dark counts in Fig. 5 are higher than the median dark count rate of 4 pixels per image without the gamma-ray source present. This could be due to several factors, including increased cross talk from higher photon collection, fluorescence from events from other particles or gamma-rays occurring before the beginning or at the end of an image's exposure time, imperfect mirror reflections, or internal reflections.

Experimental cross-validation of localization algorithm. The distances between the mean and individual estimated event locations over images with removed mirror reflections are small, demonstrating an agreement in event location measurements among different images of the same event with removed mirror reflections. This agreement indicates the algorithm is in fact measuring the event's location and not spurious light sources. The distributions of fraction of photon counts removed from an image when removing one and two mirror reflections are centered close to 1/5 and 2/5, indicating that photons from a mirror reflection are being classified correctly by the algorithm. These results would be unlikely if the algorithm were not measuring the event, or if images were of spurious light that does not originate from an event or follow the kaleidoscopic model. Further proof that the algorithm is measuring events is seen in simulations where the ground truth is known.

Simulations. The results in Tab. 1 show that the kaleidoscopic design improves 3D localization performance compared to estimating depth from defocus and attains submillimeter resolution across all brightness levels tested. The kaleidoscopic design's performance retains high accuracy and resolution even at lower brightness levels, demonstrating robustness to low photon counts and dark counts.

Limitations and future work. In this work, we only test one specific kaleidoscopic geometry with first-order reflections from one event. Future work may test different kaleidoscopic geometries and higher-order reflections. Developing a method to measure multiple events in one image would allow to construct a Compton camera or neutron scatter camera to localize the radiation source [27, 34].

Internal reflections at the scintillator's base surface could possibly appear in an image after reflecting off a mirrored surface. An internal reflection has the same effect as adding a mirror to the scintillator's base surface. Then the following reflection off the physical mirror can be modeled as a second-order reflection. Since internal reflection occurs at incidence angles higher than the critical angle, the mirror reflection of an internal reflection will exist away from first-order mirror reflections in x and y directions along the mirror's normal vector. The camera's FOV in the experiments is limited so that imaging mirror reflections that follow from internal reflections at the scintillator's base surface is infrequent. Hardware configurations with a larger camera FOV may capture internal reflections and have to account for them. Imaging internal reflections will increase light collection and image complexity.

Acknowledgments

This material is based upon work supported by the Department of Energy / National Nuclear Security Administration under Award Number(s) DE-NA0004196.

U.S. Department of Energy (Disclaimer): This work was prepared as an account of work sponsored by an agency of the United States Government. Neither the United States Government nor any agency thereof, nor any of their employees, nor any of their contractors, subcontractors or their employees, makes any warranty, express or implied, or assumes any legal liability or responsibility for the accuracy, completeness, or any third parties use or the results of such use of any information, apparatus, product, or process disclosed, or represents that its use would not infringe privately owned rights. Reference herein to any specific commercial product, process, or service by trade name, trademark, manufacturer, or otherwise, does not necessarily constitute or imply its endorsement, recommendation, or favoring by the United States Government or any agency thereof or its contractors or subcontractors. The views and opinions of authors expressed herein do not necessarily state or reflect those of the United States Government or any agency thereof, its contractors or subcontractors.

References

[1] Robert Adams and Robert Zboray. Gamma radiography and tomography with a ccd camera and co-60 source. *Applied Radiation and Isotopes*, 127:82–86, 2017. 2

[2] Byeongjoo Ahn, Ioannis Gkioulekas, and Aswin C Sankaranarayanan. Kaleidoscopic structured light. *ACM Transactions on Graphics (TOG)*, 40(6):1–15, 2021. 2

[3] Byeongjoo Ahn, Michael De Zeeuw, Ioannis Gkioulekas, and Aswin C Sankaranarayanan. Neural kaleidoscopic space sculpting. In *Proceedings of the IEEE/CVF Conference on Computer Vision and Pattern Recognition*, pages 4349–4358, 2023. 2

[4] Stuart Baker, Kristina Brown, Alden Curtis, Stephen S Lutz, Russell Howe, Robert Malone, Stephen Mitchell, Jeremy Danielson, Todd Haines, and Kris Kwiatkowski. Scintillator efficiency study with mev x-rays. In *Hard X-Ray, Gamma-Ray, and Neutron Detector Physics XVI*, pages 78–87. SPIE, 2014. 2

[5] Swathi Lakshmi Balasubramanian and Ganapathy Krishnamurthi. X-ray scintillator lens-coupled with cmos camera for pre-clinical cardiac vascular imaging—a feasibility study. *Plos one*, 17(2):e0262913, 2022. 2

[6] Shaun Bangay and Judith D Radloff. Kaleidoscope configurations for reflectance measurement. In *Proceedings of the 3rd international conference on Computer graphics, virtual reality, visualisation and interaction in Africa*, pages 161–170, 2004. 2

[7] Jonathan S Beaumont, Matthew P Mellor, Mario Villa, and Malcolm J Joyce. High-intensity power-resolved radiation imaging of an operational nuclear reactor. *Nature Communications*, 6(1):8592, 2015. 1

[8] Alex Bocchieri, Edoardo Charbon, and Andreas Velten. Scintillation event imaging with a single photon avalanche diode camera. *Communications Engineering*, 3(1):135, 2024. 2, 7, 8, 3

[9] Gabriele D'Amen, Michael Keach, Andrei Nomerotski, Peter Svihra, and Alessandro Tricoli. Novel imaging technique for α-particles using a fast optical camera. *Journal of Instrumentation*, 16(02):P02006, 2021. 2

[10] Siyu Fan, Yinhu Xi, Yingying Guo, Yifeng Zhu, Shenao Liang, Haohao Zhang, and Nan Zhang. Kaleidoscopic imaging system for three-dimensional reconstruction of wear debris. *Engineering Research Express*, 7(4):045511, 2025. 2

[11] Mykhaylo Filipenko, Timur Iskhakov, Patrick Hufschmidt, Gisela Anton, Michael Campbell, Thomas Gleixner, Gerd Leuchs, Timo Tick, John Vallerga, Michael Wagenpfeil, et al. Three-dimensional photograph of electron tracks through a plastic scintillator. *The European Physical Journal C*, 74(11):3131, 2014. 2

[12] Tianqi Gao, Gabriele D'Amen, Sergey Burdin, Mohammad Alsulimane, Paul Campbell, Cinzia Da Via, Andrei Nomerotski, Adam Roberts, Peter Svihra, Konstantinos Mavrokoridis, et al. Novel imaging technique for thermal neutrons using a fast optical camera. *Nuclear Instruments and Methods in Physics Research Section A: Accelerators, Spectrometers, Detectors and Associated Equipment*, 1046: 167604, 2023. 2

[13] Joshua Gluckman and Shree K Nayar. Planar catadioptric stereo: Geometry and calibration. In *Proceedings. 1999 IEEE Computer Society Conference on Computer Vision and Pattern Recognition (Cat. No PR00149)*, pages 22–28. IEEE, 1999. 2

[14] Joshua Gluckman and Shree K Nayar. Rectified catadioptric stereo sensors. *IEEE transactions on pattern analysis and machine intelligence*, 24(2):224–236, 2002. 2

[15] Andrea Gonzalez-Montoro, Antonio J Gonzalez, Shirin Pourashraf, Robert S Miyaoka, Peter Bruyndonckx, Garry Chinn, Larry A Pierce, and Craig S Levin. Evolution of pet detectors and event positioning algorithms using monolithic scintillation crystals. *IEEE Transactions on Radiation and Plasma Medical Sciences*, 5(3):282–305, 2021. 1, 2

[16] Alex Gustschin, Yiyong Han, Adrian Losko, Alexander Wolfertz, Daniel S Hussey, László Szentmiklósi, Zoltán Kis, Pavel Trtik, Pierre Boillat, Anders Kaestner, et al. Event-based high-resolution neutron image formation analysis using intensified cmos cameras. *Scientific Reports*, 14(1): 26941, 2024. 2

[17] Hiroki Hosokoshi, Jun Kataoka, Saku Mochizuki, Masaki Yoneyama, Soichiro Ito, Hiroaki Kiji, Fumiya Nishi, Shuji Miyamoto, and Tatsushi Shima. Development and performance verification of a 3-d position-sensitive compton camera for imaging mev gamma rays. *Scientific reports*, 9(1): 18551, 2019. 2

[18] Daniel S Hussey, Jacob M LaManna, Elias Baltic, and David L Jacobson. Neutron imaging detector with 2 μm spatial resolution based on event reconstruction of neutron capture in gadolinium oxysulfide scintillators. *Nuclear Instruments and Methods in Physics Research Section A: Acceler-*

ators, Spectrometers, Detectors and Associated Equipment*, 866:9–12, 2017. 2

[19] J Kataoka, A Kishimoto, T Nishiyama, T Fujita, K Takeuchi, T Kato, T Nakamori, S Ohsuka, S Nakamura, M Hirayanagi, et al. Handy compton camera using 3d position-sensitive scintillators coupled with large-area monolithic mppc arrays. *Nuclear Instruments and Methods in Physics Research Section A: Accelerators, Spectrometers, Detectors and Associated Equipment*, 732:403–407, 2013. 2

[20] Ryo Kawahara, Meng-Yu Jennifer Kuo, and Shohei Nobuhara. Teleidoscopic imaging system for microscale 3d shape reconstruction. In *Proceedings of the IEEE/CVF Conference on Computer Vision and Pattern Recognition*, pages 20813–20822, 2023. 2

[21] M Kawula, TM Binder, S Liprandi, R Viegas, Katia Parodi, and Peter G Thirolf. Sub-millimeter precise photon interaction position determination in large monolithic scintillators via convolutional neural network algorithms. *Physics in Medicine & Biology*, 66(13):135017, 2021. 2

[22] Hyounggun Lee, Taewoong Lee, and Wonho Lee. Development of a position-sensitive 4π compton camera based on a single segmented scintillator. *IEEE Transactions on Nuclear Science*, 67(12):2511–2522, 2020. 2

[23] AS Losko, Y Han, B Schillinger, A Tartaglione, M Morgano, M Strobl, J Long, AS Tremsin, and M Schulz. New perspectives for neutron imaging through advanced event-mode data acquisition. *Scientific reports*, 11(1):21360, 2021. 2

[24] M Menichelli, Stefano Ansoldi, M Bari, M Basset, R Battiston, S Blasko, F Coren, E Fiori, G Giannini, D Iugovaz, et al. A scintillating fibres tracker detector for archaeological applications. *Nuclear Instruments and Methods in Physics Research Section A: Accelerators, Spectrometers, Detectors and Associated Equipment*, 572(1):262–265, 2007. 1

[25] Hiroshi Mitsumoto, Shinichi Tamura, Kozo Okazaki, Naoki Kajimi, and Yutaka Fukui. 3-d reconstruction using mirror images based on a plane symmetry recovering method. *IEEE Transactions on Pattern Analysis & Machine Intelligence*, 14 (09):941–946, 1992. 2

[26] Sameer A Nene and Shree K Nayar. Stereo with mirrors. In *Sixth International Conference on Computer Vision (IEEE Cat. No. 98CH36271)*, pages 1087–1094. IEEE, 1998. 2

[27] Raj Kumar Parajuli, Makoto Sakai, Ramila Parajuli, and Mutsumi Tashiro. Development and applications of compton camera—a review. *Sensors*, 22(19):7374, 2022. 2, 8

[28] Helena Pleinert, Eberhard Lehmann, and Sonja Körner. Design of a new ccd-camera neutron radiography detector. *Nuclear Instruments and Methods in Physics Research Section A: Accelerators, Spectrometers, Detectors and Associated Equipment*, 399(2-3):382–390, 1997. 2

[29] Ilya Reshetouski, Alkhazur Manakov, Hans-Peter Seidel, and Ivo Ihrke. Three-dimensional kaleidoscopic imaging. In *CVPR 2011*, pages 353–360. IEEE, 2011. 2

[30] Krysta Ryzewski, S Herringer, H Bilheux, Lakeisha Walker, B Sheldon, S Voisin, J-C Bilheux, and V Finocchiaro. Neutron imaging of archaeological bronzes at the oak ridge national laboratory. *Physics Procedia*, 43:343–351, 2013. 1

[31] V Schonfelder, R Diehl, GG Lichti, H Steinle, BN Swanenburg, AJM Deerenberg, H Aarts, J Lockwood, W Webber, J Macri, et al. The imaging compton telescope comptel on the gamma ray observatory. *IEEE Transactions on Nuclear Science*, 31(1):766–770, 1984. 1

[32] Kosuke Takahashi and Shohei Nobuhara. Structure of multiple mirror system from kaleidoscopic projections of single 3d point. *IEEE Transactions on Pattern Analysis and Machine Intelligence*, 44(9):5602–5617, 2021. 2

[33] Kai Vetter, Ross Barnowksi, Andrew Haefner, Tenzing HY Joshi, Ryan Pavlovsky, and Brian J Quiter. Gamma-ray imaging for nuclear security and safety: Towards 3-d gamma-ray vision. *Nuclear Instruments and Methods in Physics Research Section A: Accelerators, Spectrometers, Detectors and Associated Equipment*, 878:159–168, 2018. 1

[34] Kyle Weinfurther, John Mattingly, Erik Brubaker, and John Steele. Model-based design evaluation of a compact, high-efficiency neutron scatter camera. *Nuclear Instruments and Methods in Physics Research Section A: Accelerators, Spectrometers, Detectors and Associated Equipment*, 883:115–135, 2018. 2, 8

[35] Ruilin Xu, Mohit Gupta, and Shree K Nayar. Trapping light for time of flight. In *Proceedings of the IEEE Conference on Computer Vision and Pattern Recognition*, pages 6219–6227, 2018. 2

[36] Seiichi Yamamoto, Masao Yoshino, Kei Kamada, Ryuga Yajima, Akira Yoshikawa, Kohei Nakanishi, and Jun Kataoka. Development of an ultrahigh resolution real time alpha particle imaging system for observing the trajectories of alpha particles in a scintillator. *Scientific reports*, 13(1):4955, 2023. 2